NANO LETTERS
Letter
Cite This: Nano Lett. 2019, 19, 6005−6012
pubs.acs.org/NanoLett

Unidirectional Spin−Orbit Interaction Induced by the Line Defect in Monolayer Transition Metal Dichalcogenides for High-Performance Devices

Xiaoyin Li,[†,§] Shunhong Zhang,[‡,§] Huaqing Huang,[§] Lin Hu,[§,∥] Feng Liu,[*,§] and Qian Wang[*,†]

[†]Center for Applied Physics and Technology, Department of Materials Science and Engineering, HEDPS, College of Engineering, Peking University, Beijing 100871, China

[‡]International Center for Quantum Design of Functional Materials (ICQD), Hefei National Laboratory for Physical Sciences at Microscale, University of Science and Technology of China, Hefei, Anhui 230026, China

[§]Department of Materials Science and Engineering, University of Utah, Salt Lake City, Utah 84112, United States

[∥]Beijing Computational Science Research Center, Beijing 100193, China

Supporting Information

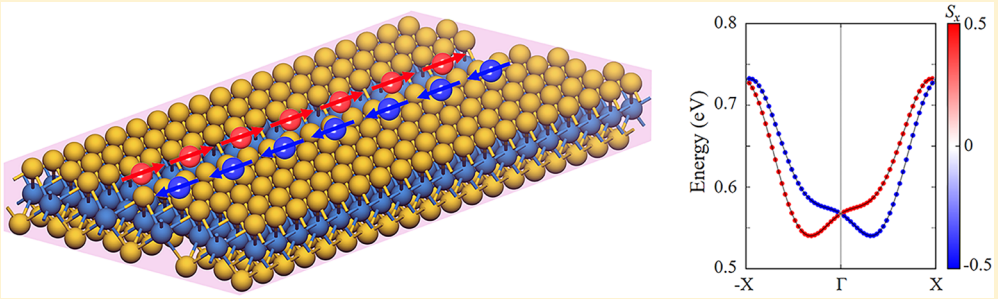

ABSTRACT: Spin−orbit (SO) interaction is an indispensable element in the field of spintronics for effectively manipulating the spin of carriers. However, in crystalline solids, the momentum-dependent SO effective magnetic field generally results in spin randomization by a process known as the Dyakonov−Perel spin relaxation, leading to the loss of spin information. To overcome this obstacle, the persistent spin helix (PSH) state with a unidirectional SO field was proposed but difficult to achieve in real materials. Here, on the basis of first-principles calculations and tight-binding model analysis, we report for the first time a unidirectional SO field in monolayer transition metal dichalcogenides (TMDs, MX_2, M = Mo, W; and X = S, Se) induced by two parallel chalcogen vacancy lines. By changing the relative positions of the two vacancy lines, the direction of the SO field can be tuned from ***x*** to ***y***. Moreover, using ***k*·*p*** perturbation theory and group theory analysis, we demonstrate that the emerging unidirectional SO field is subject to both the structural symmetry and 1D nature of such defects engineered in 2D TMDs. In particular, through transport calculations, we confirm that the predicted SO states carry highly coherent spin current. Our findings shed new light on creating PSH states for high-performance spintronic devices.

KEYWORDS: *Persistent spin helix state, monolayer TMDs, line defect, spin−orbit coupling, spin transistor*

Spintronics, utilizing the spin degree of freedom of carriers, has already been widely investigated for spin information processing and quantum computing technologies.[1] In addition to effective spin manipulation, long spin lifetime is also desirable in spintronic devices. The spin−orbit coupling (SOC) effect, arising from the interaction between a carrier's spin and its motion, provides a practical recipe to manipulate spin states in the absence of an external magnetic field. However, in solids, the direction of the SO field is generally momentum-dependent, resulting in spin randomization by the Dyakonov−Perel spin relaxation mechanism,[2] which is detrimental for spin lifetime and limits the performance of spintronic devices. To solve this problem, the persistent spin helix (PSH) state has been proposed theoretically[3,4] and realized experimentally,[5,6] where the orientation of the SO field is unidirectional and momentum-independent. To date, most schemes to realize PSH states rely on precise control of the relative strength of the Rashba[7] and Dresselhaus[8] SO interactions in III−V semiconductor quantum wells.[9−13] When the strengths of the Rashba and the Dresselhaus SOC become equal ($\lambda_R = \lambda_D$), the combined SO field is aligned in a uniaxial direction with SU(2) symmetry, which is robust against spin-independent scattering and renders the spin lifetime ultimately infinite.[3,4] Despite the advantages of the PSH states, the stringent condition of $\lambda_R = \lambda_D$ is difficult to satisfy because it requires matched quantum well width and

Received: May 3, 2019
Revised: August 3, 2019
Published: August 6, 2019

DOI: 10.1021/acs.nanolett.9b01812
Nano Lett. 2019, 19, 6005−6012

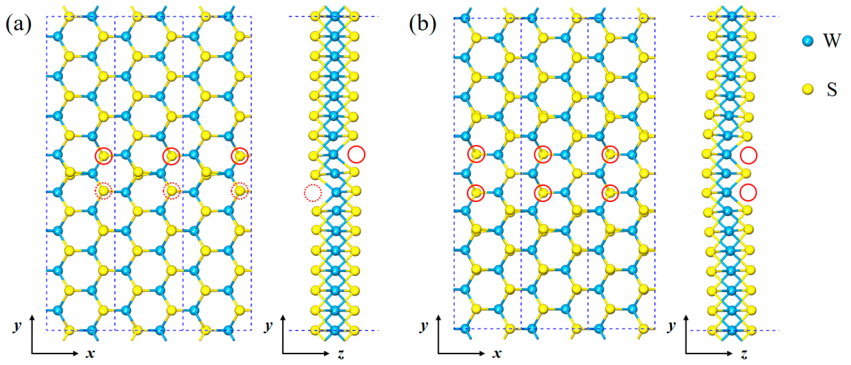

Figure 1. Top and side views of the optimized structures of WS_2 with two parallel aligned S vacancy line defects residing in (a) the opposite sides (DLD-I) and (b) the same side (DLD-II) of the monolayer, respectively. The blue dashed lines outline the rectangle lattices; the red solid and dashed circles represent S vacancies located on the top and bottom side of the monolayer, respectively.

doping level as well as the application of an external gate bias, which limit the applications of the PSH states to realistic devices.[14,15] Additionally, it has been demonstrated that the PSH states can also be achieved in specific noncentrosymmetric bulk materials where the PSH state is enforced by the nonsymmorphic space group symmetry of the crystal.[16] However, these states survive only along certain high-symmetry paths in the Brillouin zone and are likely overwhelmed by other non-PSH states in the same energy window, which severely hamper their practical applications. Therefore, it is highly desirable to explore new methods and material platforms for realizing the PSH states that are completely separated from other states and support coherent spin transport.

Electronic states formed inside the band gap of a semiconductor due to crystal defects are usually detrimental to bulk properties.[17−20] However, from a positive perspective, these midgap states can be isolated from bulk bands, providing the opportunity to realize the ideal PSH states. Remarkably, a recent study has demonstrated that screw dislocation (SD) in semiconductors presents a new form of SOC states (SD-SOC), which reside in the band gap of semiconductors and are completely separated from the bulk bands.[21] More importantly, the SD-SOC has a much higher degree of spin coherency, which is tunable in terms of the ionicity of the compound semiconductor. Specifically, in compound semiconductors with medium ionicity, like SiC, the spin vector of the SD-SOC state is fixed in the [110] direction which presents an exactly unidirectional SO field. However, formation of screw dislocations can be difficult to control in three-dimensional (3D) bulk materials, limiting its application in future nanodevices and integrated spintronic devices in spite of the novelty of the SD-SOC. This motivates us to search for the unique unidirectional SO field in materials with a reduced dimensionality by introducing defects that preserve specific symmetry.

Specifically, we turn our attention to two-dimensional (2D) materials with atomic thickness and high exposure of surface atoms, which allows for easy regulation of properties by means of defect engineering.[22] Among the vast family of 2D materials, we focus on the 1H phase ("1H" refers to a monolayer exfoliated from the bulk 2H phase) of monolayer transition metal dichalcogenides (TMDs) MX_2 (M = Mo, W; and X = S, Se) for three critical reasons. First, these 2D materials are robust in the environment, and their fabrication (by epitaxial growth or exfoliation) and controllable defects engineering have been experimentally realized.[23−25] Second, they are all semiconductors with a moderate band gap (∼1−2 eV),[26−28] providing the possibility to create ideal SOC states free of interference from bulk states. Third, the SOC strength is quite large in these materials,[29] enabling effective manipulation of spin states. In light of these merits, using first-principles calculations combined with group theory analysis, we discover two types of unidirectional SO fields in the monolayer TMDs engineered by two parallel aligned chalcogen vacancy lines. The orientation of the SO field can be tuned from the $\boldsymbol{x}$ (parallel to the line defect) to $\boldsymbol{y}$ (normal to the line defect) direction by changing the relative positions of the two vacancy lines. Considering that the physics in these MX_2 monolayers is essentially the same, we use the WS_2 monolayer as an example to illustrate the emerging properties and the underlying mechanism of the unique SO field, and the results of the other three monolayers are presented in the Supporting Information. In the following, for simplicity we use MX_2 to represent the MX_2 monolayer unless stated otherwise.

Our first-principles calculations within the framework of density functional theory (DFT) are performed using the Vienna ab initio simulation package (VASP).[30] The projector augmented wave (PAW) pseudopotential[31] is used to treat interactions between ion cores and valence electrons, with a kinetic energy cutoff of 350 eV. The Perdew−Burke−Ernzerhof (PBE) functional with the generalized gradient approximation (GGA)[32] is adopted to treat the electron exchange-correlation interactions. The Brillouin zone is meshed following the Monkhorst−Pack scheme[33] with a k grid density of $2\pi \times 0.03$ Å^{-1}, i.e., a $7 \times 2 \times 1$ k-mesh. A large vacuum space of ∼20 Å in the direction perpendicular to the monolayer is placed to eliminate interactions between periodic layers. Lattice constants and atomic positions are fully relaxed, and the energy and force convergence criteria are set to be 10^{-4} eV and 10^{-2} eV/Å, respectively. The spin-dependent charge transport calculations are performed using Kwant code.[34]

MX_2 (M = Mo, W; and X = S, Se) with a 1H structure is composed of a sandwich of three planes, that is, a transition metal (M) layer sandwiched by two chalcogen (X) layers. In each plane atoms pack triangularly, and three planes stack in the Bernal (ABA) sequence forming a honeycomb lattice. In this work, the proposed chalcogen vacancy line defects are oriented along the armchair direction of MX_2, and the two parallel aligned line defects are separated by a single atomic line, as shown in Figure 1, where the relaxed structures of WS_2

DOI: 10.1021/acs.nanolett.9b01812
Nano Lett. 2019, 19, 6005−6012

are displayed as examples. We notice that the aggregation of sulfur vacancies and their alignment into extended line defects in MoS_2 through electron irradiation has been characterized experimentally,[35,36] and the orientation of the line defect is sensitive to mechanical strain,[24] implying the feasibility of experimental realization of our proposed line defects through a combination of electron irradiation and strain. Furthermore, it was reported that scanning probe microscopes can achieve controllable detachment of sulfur atoms from the surface of cleaved MoS_2,[37,38] providing another manageable approach to create line defects with a designed pattern. In our simulation, to eliminate interactions between periodic images of line defects, we extend the cell size by 8 times in the direction perpendicular to the line defects, which is confirmed to be enough to converge the result (see Figure S1 in the Supporting Information). We consider two typical configurations of double line defects (DLDs) in WS_2: in Figure 1a, the two line defects reside on the opposite sides of the monolayer, while those in Figure 1b are located on the same side of the monolayer. We name the DLDs in Figure 1a,b as DLD-I and DLD-II, respectively. To assess the stability of the proposed DLDs, we calculate their formation energy and phonon dispersion and perform ab initio molecular dynamics simulations at 300 K. The results summarized in the Supporting Information confirm the energetic, dynamic, and thermal stability of the defective structures.

Figure 2a,b shows the calculated band structures and projected density of states (PDOS) of WS_2 embedded with DLD-I and DLD-II, respectively, without including SOC. According to spin-polarized calculations, there is no lift of the spin degeneracy in any eigenstate and no spin density accumulation in real space, indicating that the DLD-I and DLD-II engineered WS_2 remain nonmagnetic as the defect-free one. In both cases, there occur several in-gap states induced by defects. These results are in good agreement with previous calculations,[39,40] where a chalcogen vacancy gives rise to a single occupied defect state in the valence bands and two unoccupied defect states in the bulk band gap of 1H MX_2. Here in our models, each unit cell contains two chalcogen vacancies to have two occupied states near the band edge and four unoccupied states in the band gap. Meanwhile, according to the PDOS, the defect states are primarily from transition metal *d* orbitals, agreeing well with previous studies.[39,40] More importantly, a single chalcogen vacancy is known to introduce nearly dispersionless midgap states with a large electron effective mass and strong localization surrounding the vacancy site, which lowers charge mobility significantly and is detrimental to charge transport by the hopping mechanism.[41] In contrast, in our proposed structures, the interactions between neighboring vacancies result in dispersive midgap states. The calculated charge density for the conduction band of DLD engineered WS_2 (see Figure S4) also shows that electrons are delocalized along the defect line, forming a quasi-1D conducting channel, implying a bandlike charge transport and higher mobility of these defect states.[42]

When including SOC, the spin degeneracy of defect states is lifted, and large band splitting occurs as shown in Figure 2c,d. Among these in-gap defect states, the conduction bands located right above the Fermi energy are completely isolated from others, in both DLD-I and DLD-II configurations (the bands marked by blue dashed boxes in Figure 2c,d). These bands provide ideal platforms for exploring the ideal SOC states. Also, utilizing the bands near the Fermi energy for charge/spin transport is more feasible from the experimental point of view. Therefore, in the following we will concentrate on these conduction bands of the DLD engineered WS_2.

We first determine the spin textures of these bands. For a given $\boldsymbol{k}$ point, its spin polarization of each eigenstate $\psi(\boldsymbol{k})$ is defined as $S(\boldsymbol{k}) = [S_x(\boldsymbol{k}), S_y(\boldsymbol{k}), S_z(\boldsymbol{k})]$, where $S_i(\boldsymbol{k}) = \langle\psi(\boldsymbol{k})|\sigma_i|\psi(\boldsymbol{k})\rangle$ is the i-direction component, and σ_i is a Pauli matrix ($i = x, y, z$). Figure 3a presents the spin-projected conduction bands of the DLD-I engineered WS_2 where the expectation value of each spin component is clearly shown. One can see that spin components of S_y and S_z are both zero, and the only nonzero spin component is S_x along the entire path of Γ−X. This suggests that the conduction bands of the DLD-I engineered WS_2 have uniaxial spin polarizations oriented along the $\boldsymbol{x}$ direction, which forms exactly the desired unidirectional SO field. The corresponding spin textures are schematically plotted in Figure 3c. Interestingly, when the relative positions of double line defects change, spin polarizations of the conduction bands also become different. Figure 3b shows the results for the DLD-II engineered WS_2, where the S_x and S_z spin components disappear while the S_y spin component is preserved. Thus, although spin polarizations in the DLD-II engineered WS_2 differ from those in the DLD-I engineered WS_2, they are both unidirectional. The corresponding spin textures along the $\boldsymbol{y}$ direction are shown in Figure 3d. Therefore, from DFT calculations, we discover that both DLD-I and DLD-II can induce the unidirectional SO field in WS_2, and the direction of the field changes from $\boldsymbol{x}$ to $\boldsymbol{y}$ by changing the relative positions of the double line defects from the opposite sides to the same side of WS_2.

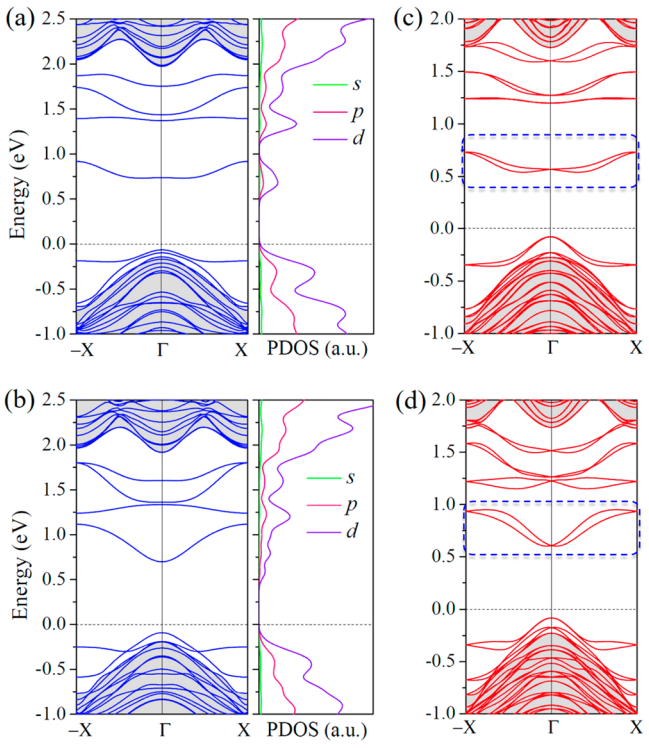

Figure 2. Band structures and PDOS of (a) DLD-I and (b) DLD-II engineered WS_2 excluding SOC. (c, d) Band structures of DLD-I and DLD-II engineered WS_2 including SOC. The Fermi energy is set to zero, and the bulk bands are marked in the shadowed region.

DOI: 10.1021/acs.nanolett.9b01812
Nano Lett. 2019, 19, 6005−6012

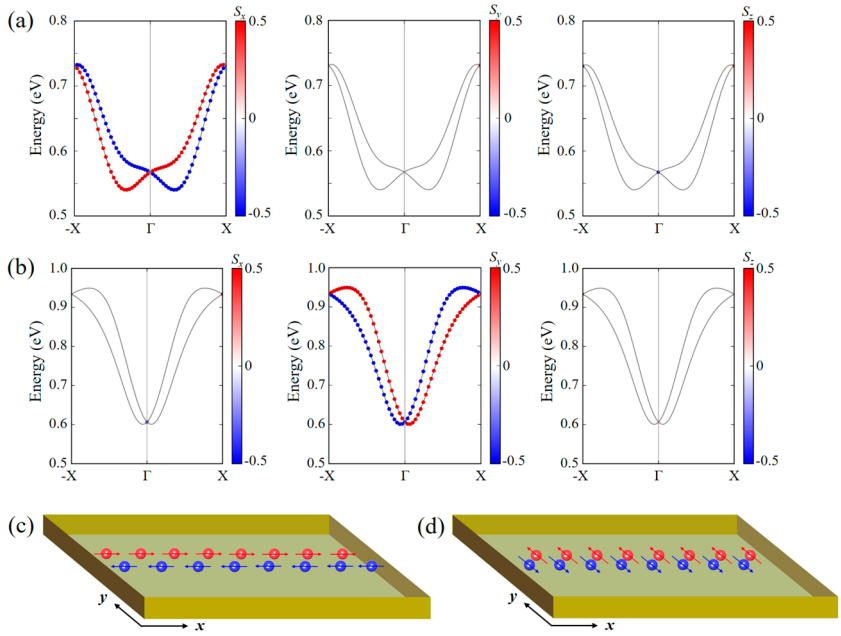

Figure 3. Spin-projected conduction bands of (a) DLD-I and (b) DLD-II engineered WS_2. Color bars represent expectation values of S_x, S_y, and S_z. (c, d) Spin textures of the conduction bands of DLD-I and DLD-II engineered WS_2.

To reveal the origin of the unidirectional SO field observed in the DLD-I and DLD-II engineered WS_2, we use $\boldsymbol{k}\cdot\boldsymbol{p}$ perturbation theory combined with group theory analysis to deduce effective SOC Hamiltonians of these conduction bands.[43] It is known that inversion symmetry breaking and spin splitting already exist in pristine WS_2 with D_{3h} point group symmetry.[29] In the presence of DLDs, the structural symmetry is further reduced. Since time reversal symmetry remains in the DLD engineered structures, the spin degeneracy (Kramers' degeneracy) is conserved at the Γ (0, 0, 0) and X (±0.5, 0, 0) points. Away from these time-reversal-invariant points, the Kramers doublet splits due to SO interaction, whose Hamiltonian can be described by a $\boldsymbol{k}\cdot\boldsymbol{p}$ Hamiltonian. Here, to derive the effective SOC Hamiltonian we first focus on the proximity of the Γ point and then extend to the entire path of Γ−X, where the symmetry group is the same as that of the Γ point.

In the case of the DLD-I engineered WS_2, the structural symmetry is reduced to C_2, which only consists of the identity operation E and a 2-fold rotation C_2 around the $\boldsymbol{x}$ axis. On the basis of the character table of C_2, we sort out the components of wave vector $\boldsymbol{k}$ and Pauli matrix $\boldsymbol{\sigma}$ according to irreducible representations as A: k_x, σ_x; B: k_y, k_z, σ_y, σ_z, since $\boldsymbol{k}$ and $\boldsymbol{\sigma}$ can be transformed as polar and axial vectors, respectively. According to the table of direct products of C_2, the combinations that are in first-order of $\boldsymbol{k}$ and belong to the A irreducible representation are $k_x\sigma_x$, $k_y\sigma_y$, $k_y\sigma_z$, $k_z\sigma_y$, and $k_z\sigma_z$. Collecting all these terms, we obtain the effective SOC Hamiltonian near the Γ point as

$$H_{so}^{C_2}(\boldsymbol{k}) = \alpha_1^1 k_x\sigma_x + \alpha_1^2 k_y\sigma_y + \alpha_1^3 k_y\sigma_z + \alpha_1^4 k_z\sigma_y + \alpha_1^5 k_z\sigma_z \quad (1)$$

where α_1 is a linear-in-$\boldsymbol{k}$ SOC parameter. However, because of the one-dimensional (1D) nature of the conduction states (distributed along the line defect which extends in the $\boldsymbol{x}$ direction), all the terms vanish except the first one in eq 1. Therefore, we obtain the effective SOC Hamiltonian of the DLD-I engineered WS_2 near the Γ point as $H_{so}^{C_2}(\boldsymbol{k}) = \alpha_1^1 k_x\sigma_x$, demonstrating that the spin textures around the Γ point are unidirectional and oriented along the $\boldsymbol{x}$ direction. When moving away to the k-points far from the Γ point, higher-order terms of the $\boldsymbol{k}\cdot\boldsymbol{p}$ model should be included. However, whatever the order of $\boldsymbol{k}$ is, the only nonzero spin component is always σ_x due to the 1D nature of such defect states in the DLD-I engineered WS_2 (details can be found in the Supporting Information), attesting that the $\boldsymbol{x}$-oriented unidirectional effective magnetic field induced by the SO interaction survives over the entire Γ−X path. This hallmark endows our proposed defect-engineering scheme with a distinct advantage over the previously widely studied III−V semiconductor-quantum-well-based unidirectional SOC field, which can only be preserved in the vicinity of the Γ point and becomes momentum-dependent when high-order terms have a considerable effect at large wave vectors. The SOC parameter of the linear term can be obtained by fitting the DFT bands, which yields $\alpha_1^1 = 0.142$ eV Å. With this parameter, one can estimate the wavelength of the PSH state around the conduction band minimum (CBM) using the formula $l_{PSH} = (\pi\hbar^2)/(m^*\alpha_1^1)$.[16] Here, m^* is the carrier effective mass calculated by fitting the band dispersion around the CBM. We obtain $m^* = 1.96m_0$ for the DLD-I engineered WS_2, with m_0 the electron rest mass. The derived wavelength is $l_{PSH} = 85.6$ Å, which characterizes the spatially periodic mode of spin polarization of the PSH state.

Next, we apply a similar analysis to the DLD-II engineered WS_2, where the structural symmetry is reduced to C_s containing the identity operation E and a mirror operation M_y: $y \rightarrow -y$. According to the character table and the direct product table of C_s, the components of $\boldsymbol{k}$ and $\boldsymbol{\sigma}$ are classified as A': k_x, k_z, σ_y; A'': k_y, σ_x, σ_z, and their combinations in the first order of $\boldsymbol{k}$ that correspond to the A' irreducible representation are $k_x\sigma_y$, $k_y\sigma_x$, $k_y\sigma_z$, and $k_z\sigma_y$. Then, we obtain the effective SOC Hamiltonian near the Γ point as

$$H_{so}^{C_s}(\boldsymbol{k}) = \alpha_1^1 k_x\sigma_y + \alpha_1^2 k_y\sigma_x + \alpha_1^3 k_y\sigma_z + \alpha_1^4 k_z\sigma_y \quad (2)$$

DOI: 10.1021/acs.nanolett.9b01812
Nano Lett. 2019, 19, 6005−6012

Similarly, because of the 1D nature of the conduction states in the DLD-II engineered WS_2, all the terms containing k_y and k_z vanish except for the k_x term in eq 2. Herein, we derive the effective SOC Hamiltonian of the DLD-II engineered WS_2 near the Γ point as $H_{so}^{C_s}(\boldsymbol{k}) = \alpha_1^1 k_x \sigma_y$, confirming that the spin textures around the Γ point are unidirectional and oriented along the $\boldsymbol{y}$ direction. Moreover, when considering high-order terms of the $\boldsymbol{k}\cdot\boldsymbol{p}$ model, the only nonzero spin component is σ_y no matter what the order of $\boldsymbol{k}$ is, indicating that the $\boldsymbol{y}$-oriented unidirectional SO field persists along the whole Γ−X path. The fitted SOC parameter of the linear term for the DLD-II engineered WS_2 is α_1^1 = 0.261 eV Å. Combined with m^* = $0.90m_0$, we derive the wavelength of the PSH state around the CBM to be l_{PSH} = 101.8 Å. It is important to emphasize that the 1D nature of the defect states is vital to the emerging unidirectional SO field, which is evidentially shown by analyzing the spin-projected band structure of DLD engineered WS_2 in a larger energy window (see Figure S5), where all the defect states that are localized around the 1D defect line exhibit a perfect uniaxial spin component, whereas the higher conduction bands that originated from the bulk states of pristine WS_2 are delocalized in the 2D xy plane possessing nonzero spin components along other directions.

Thus far, we have demonstrated that the unidirectional SO field in the DLD engineered WS_2 is subject to both the structural symmetry and the 1D nature of the defect states. In principle, the effective $\boldsymbol{k}\cdot\boldsymbol{p}$ model can also describe the band dispersion as well as the unidirectional feature of the SO field throughout the Brillouin zone if substantial perturbative terms are included to expand the Hamiltonian. Nevertheless, to better understand the electronic and spin-dependent properties of these SOC states, in the following we show simulations of spin transport properties. From Figure 2c,d, we know that the studied conduction bands are completely separated from other bands in energy. Moreover, the calculated charge density distribution of these bands is localized around the defect line (see Figure S4). Thus, we can construct a single-orbital tight-binding (TB) Hamiltonian and only consider hopping along the line defects to capture the essential physics of the defect-induced conduction bands. By including the nearest-neighbor (NN) and next-NN (NNN) hoppings and taking SO interaction into account, the 2 × 2 TB model Hamiltonian of the DLD-I engineered WS_2 reads as

$$H = \begin{pmatrix} \varepsilon + 2t_1\cos(ak_x) + 2t_2\cos(2ak_x) & -2\alpha\sin(ak_x) \\ -2\alpha\sin(ak_x) & \varepsilon + 2t_1\cos(ak_x) + 2t_2\cos(2ak_x) \end{pmatrix} \quad (3)$$

where ε is the on-site energy, t_1 and t_2 are the NN and NNN hopping parameters, α is the SOC parameter, and a is the lattice constant in the $\boldsymbol{x}$ direction. The model parameters can be derived by fitting the TB bands to the DFT results. We present the band structures of the DLD-I engineered WS_2 calculated using the TB model in Figure 4a and list the corresponding model parameters in Table 1. The band structures obtained by the TB model and DFT calculations agree well. For the DLD-II engineered WS_2, the nonzero spin component is σ_y, and its TB model Hamiltonian is written as

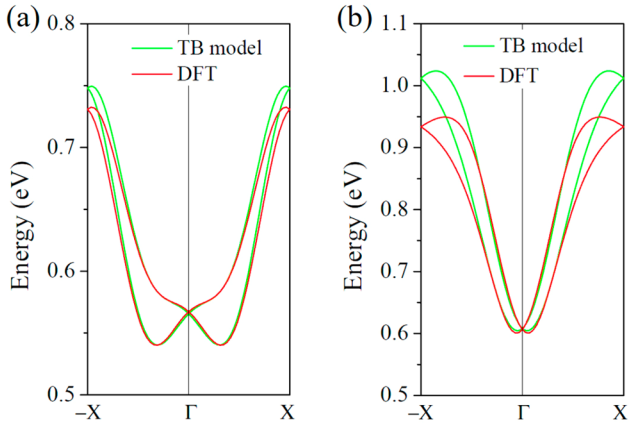

Figure 4. Comparison of band structures obtained by the TB model and DFT calculations for (a) DLD-I and (b) DLD-II engineered WS_2.

Table 1. Values of On-Site Energy ε, Hopping Parameters t_1 and t_2, SOC Parameter α, and Lattice Constant a in DLD-I and DLD-II Engineered WS_2

	ε (eV)	t_1 (eV)	t_2 (eV)	α (eV)	a (Å)
DLD-I	0.625	−0.046	0.016	0.013	5.461
DLD-II	0.839	−0.101	−0.015	0.024	5.441

$$H = \begin{pmatrix} \varepsilon + 2t_1\cos(ak_x) + 2t_2\cos(2ak_x) & 2i\alpha\sin(ak_x) \\ -2i\alpha\sin(ak_x) & \varepsilon + 2t_1\cos(ak_x) + 2t_2\cos(2ak_x) \end{pmatrix} \quad (4)$$

where ε, t_1, t_1, α, and a have the same meanings as those in eq 3. By fitting the TB bands with the DFT results, we obtain the model parameters of the DLD-II engineered WS_2, as listed in Table 1. The TB bands are shown in Figure 4b, also reproducing satisfactorily the results of DFT calculations.

Historically, the first SOC-based spintronic device is the spin transistor taking advantage of the Rashba SOC as proposed by Datta and Das;[44] then, the nonballistic spin transistor based on the unidirectional SOC was proposed by Schliemann et al., being tolerant against spin-independent scattering processes.[3] In practice, the operation of spin transistors relies on the modulation of spin-dependent current detected by the drain. Therefore, to investigate the possible spintronic applications of the DLD engineered MX_2, it is useful to investigate their spin-dependent transport properties. Here, using the two defected WS_2 systems as illustrations, we calculate the spin-dependent conductance with the aid of the above-constructed TB model Hamiltonian. A two-terminal device setup for the transport calculation is schematically shown in Figure 5a. The left and right leads are both ferromagnets without SOC, acting as the source and drain. The central region uses the DLD engineered WS_2 as the conducting channel. Setting spins in the left lead in the up configuration while those in the right lead in the up or down configuration, one can obtain the spin up−up and up−down conductance, respectively. Since we concentrate on intrinsic transport properties without including interfacial effects between the lead and conducting channel, we use the same Hamiltonians to model the source/drain and central conducting region. However, to capture the ferromagnetic and non-SOC features of leads, several modifications are made to the left/right lead Hamiltonian. To exclude SOC in the lead regions, we first set the spin-flip elements in the lead

DOI: 10.1021/acs.nanolett.9b01812
Nano Lett. 2019, 19, 6005−6012

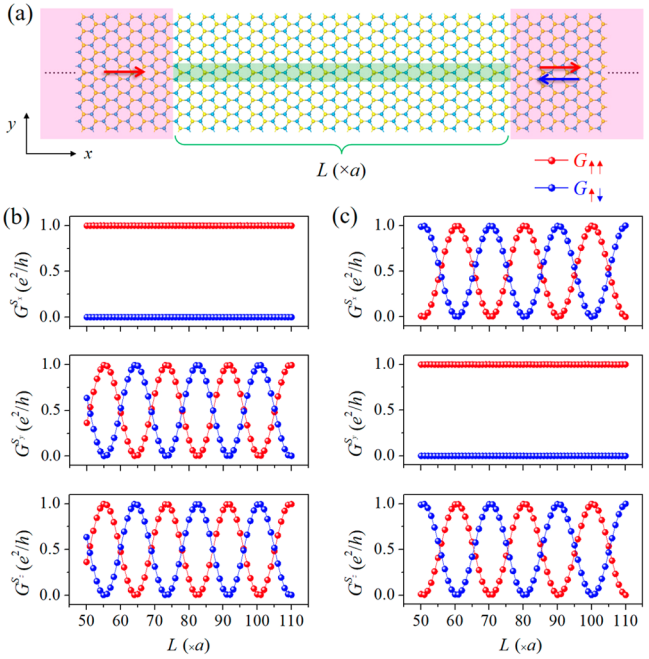

Figure 5. (a) Schematic nanoribbon device setup to measure spin-dependent conductance. The nanoribbon width is ∼25 Å, containing one DLD. The left and right shadowed regions represent the source and drain leads, which are ferromagnetic and without SOC. Their spins (shown in arrows) aligned either parallel or antiparallel. Here, spin oriented along the x direction is shown as an example. The central region is the conducting channel with SOC, where the green shaded rectangle represents the DLD responsible for the PSH state. (b, c) Spin-dependent conductance as a function of channel length (L, in units of lattice constant a) at energy E = 0.65 eV for DLD-I and DLD-II engineered WS_2, respectively. Here, H_0 = 0.001 eV.

Hamiltonian matrix to zero. To mimic the ferromagnetic properties of leads, we include a Zeeman splitting term to the lead Hamiltonian

$$H_z = H_0 \begin{pmatrix} \frac{e^{i\theta} + e^{-i\theta}}{2} & e^{-i\varphi} \\ e^{i\varphi} & \frac{-e^{i\theta} - e^{-i\theta}}{2} \end{pmatrix} \quad (5)$$

where H_0 represents the strength of the magnetic field, and (θ, φ) describes the direction of magnetization. θ ($0 \le \theta \le \pi$) is the angle between the magnetization direction and the $+z$ axis, while φ ($0 \le \varphi \le 2\pi$) is the angle between the magnetization direction and the $+x$ axis. Hence, ($\pi/2$, 0)/($\pi/2$, π) represents the magnetization along the $\pm x$ axis; ($\pi/2$, $\pi/2$)/($\pi/2$, $3\pi/2$) the magnetization along the $\pm y$ axis; and (0, 0)/(π, 0) the magnetization along the $\pm z$ axis.

Using the above device Hamiltonian, we then calculate its spin-dependent ballistic conductance through the Landauer–Büttiker formalism[45]

$$G^{S_i}(E) = \frac{e^2}{h} T^{S_i} = \frac{e^2}{h} \mathrm{Tr}[\sigma_i \Gamma_L G_R(E)\, \Gamma_R G_A(E)] \quad (6)$$

which relates the conductance G of a device to its transmission coefficient T. Here, $\Gamma_{L/R}$ represents the interaction between the central conducting region and the left/right lead, defined as $\Gamma_{L/R} = i[\Sigma_{L/R} - \Sigma_{L/R}^{\dagger}]$, where $\Sigma_{L/R}$ is the retarded self-energy. $G_{R/A}(E)$ is the retarded/advanced Green's function at energy E, defined as $G_R(E) = [H - (E + i\eta) + \Sigma_L + \Sigma_R]^{-1}/G_A(E) = [G_R(E)]^{\dagger}$, with H being the Hamiltonian of the system and η being an infinitesimally small number. By setting the magnetization direction of the left and right leads along the x, y, or z axis, we calculate the corresponding spin-dependent conductance G^{S_x}, G^{S_y}, and G^{S_z} of the device. Figure 5b shows the results of the DLD-I engineered WS_2. One can see that the spin-dependent conductance (G^{S_x}) is quantized against the channel length L when spin polarizations of the injected electrons are along the $+x$ axis. However, when the injected electrons are spin-polarized along the $+y$ or $+z$ axis, the spin-dependent conductance (G^{S_y}/G^{S_z}) as a function of L exhibit a perfect oscillation with periodicity of ∼18a. These results are consistent with the above discussions regarding the SO field in the DLD-I engineered WS_2, where the effective magnetic field induced by SOC is unidirectional and x-oriented. Under this condition, injected electrons in S_x spin states transverse the channel region with their spin states unchanged, leading to quantized G^{S_x}. However, when injected electrons are in S_y or S_z spin states, their spins precess as they travel through the channel region due to the torque from the effective magnetic field, resulting in oscillated G^{S_y} and G^{S_z}, which is exactly the resultant of the so-called PSH. The oscillation periodicity for the conductance is the wavelength of the PSH state at that Fermi energy. Therefore, we calculate the corresponding PSH wavelength via $\lambda_{PSH} = 2\pi/\Delta k$ to quantitatively explain the origin of conductance oscillation periodicity, where Δk is the wave vector shift of up and down spins at the Fermi energy.[46] Solving the TB model at the selected Fermi energy (E = 0.65 eV in the transport simulation), we obtain Δk = 0.0633 Å^{-1} for the DLD-I engineered WS_2. Then, the wavelength λ_{PSH} is calculated to be 99.3 Å, which is consistent with the transport simulation result of $\lambda_{PSH} = 18 \times a$ = 98.3 Å. As for the case of the DLD-II engineered WS_2, we obtain similar conductance results as shown in Figure 5c. However, because the SO interaction induced effective magnetic field in the DLD-II engineered WS_2 is along the y direction, quantized spin-dependent conductance appears when injected electrons are in S_y spin states, while oscillated spin-dependent conductance occurs with a periodicity of ∼20a when electrons with S_x or S_z spin states are injected. Similarly, we derive Δk = 0.0578 Å^{-1} and λ_{PSH} = 108.7 Å at E = 0.65 eV for the DLD-II engineered WS_2, which also agrees well with the transport simulation result of $\lambda_{PSH} = 20 \times a$ = 108.8 Å.

The unique spin-dependent transport properties of the DLD engineered WS_2 imply their promising applications in the field of spintronics. In particular, since spin relaxation is effectively suppressed in these systems, they can transport coherent spin information for a long distance in spintronic devices. Additionally, another device realization of the DLD engineered WS_2 is the spin transistor as shown in Figure 5a. Once the magnetization of the left lead is fixed to ensure that injected electrons are in one of the k-independent spin states ($\pm S_x/\pm S_y$ spin states for DLD-I/DLD-II engineered WS_2), the on/off state of the device corresponds to the parallel/antiparallel magnetic configuration of the right lead. The magnetization direction of the left/right lead can be tuned by a local external magnetic field.[47] Moreover, the performance of the proposed spin transistor should be robust against spin-independent disorders and impurities, as that proposed by Schliemann et al.[3]

In addition to the spin-dependent current measurement, there may be some alternative approaches to detect the

DOI: 10.1021/acs.nanolett.9b01812
Nano Lett. 2019, 19, 6005−6012

unidirectional spin texture predicted in this work. For example, if one tunes the Fermi energy to lie within the band gap of the defective system rather than to cross the PSH states and uses the system as a tunnel barrier of a tunnel junction, then the transport will switch to the tunneling regime. Consequently, the type of spin texture of the barrier region (e.g., the DLD engineered WS_2) could be confirmed by studying the tunneling spin Hall effect or anomalous Hall effect of the junction, which has been used in previous works.[48−50]

To further demonstrate the generality of our idea, we have also systematically implemented our strategy to other TMDs (MoS_2, $MoSe_2$, and WSe_2) engineered by double line defects and obtained similar unidirectional SO fields but a different SOC strength (see the Supporting Information for details). Note that the key of our scenario is to manipulate the SO field by eliminating undesired terms from the SO Hamiltonian, and defect engineering only represents one viable approach. Practically, chemical functionalization or a superlattice may also reach this goal. Other emergent 2D materials with considerable SOC can also serve as the candidate materials. It is worth mentioning that, when advancing the proposed theoretical model to materials realization and device application, many practical issues should be considered. For example, the defect sites are usually chemically more reactive than the normal sites, which might lead to chemisorption of extrinsic atoms or radicals detrimental to the PSH state. To mitigate this concern, we propose a sandwiching scheme to protect the proposed PSH state. The ideal band alignments (Figure S12) indicate that the BN monolayer is a promising material to prevent the system from air passivation and to maintain the ideal PSH state of the DLD engineered TMDs.

In conclusion, combining first-principles calculations with group theory analysis, we demonstrate two types of ideal PSH states in monolayer TMDs induced by parallel aligned double line defects. The emerging unidirectional SO field is subject to both the structural symmetry and 1D nature of the line defects. Moreover, the orientation of the SO field can be effectively tuned by altering the line defect spatial distribution, namely, the SO field oriented parallel/perpendicular to the line defects when the two line defects reside in the opposite sides/the same side of the TMD monolayer. Our findings provide a new path to achieving the long-sought PSH states, which would motivate further theoretical and experimental efforts on applying exotic SOC states for high-performance spintronic devices.

■ ASSOCIATED CONTENT

Supporting Information

The Supporting Information is available free of charge on the ACS Publications website at DOI: 10.1021/acs.nanolett.9b01812.

Additional data and figures including analysis of high-order SOC terms in the $k \cdot p$ model; band structures; stability analysis; charge density distribution; spin-projected band structure; band structures; spin components; optimized structures; TB model parameters; TB bands; and sandwiching scheme (PDF)

■ AUTHOR INFORMATION

Corresponding Authors

*E-mail: fliu@eng.utah.edu.
*E-mail: qianwang2@pku.edu.cn.

ORCID

Shunhong Zhang: 0000-0003-2120-4574
Huaqing Huang: 0000-0002-0283-8603
Feng Liu: 0000-0002-3701-8058
Qian Wang: 0000-0002-9766-4617

Notes

The authors declare no competing financial interest.

■ ACKNOWLEDGMENTS

This work is partially supported by grants from the National Key Research and Development Program of the Ministry of Science and Technology of China (Grants 2016YFE0127300 and 2017YFA0205003), and the National Natural Science Foundation of China (Grant NSFC-21773004). X.L. acknowledges funding from the Graduate School of Peking University that enabled her to visit Professor Feng Liu's group at University of Utah and carry out most of the present work. H.H. and F.L. acknowledge support by U.S. DOE-BES (Grant DE-FG02-04ER46148). Computations of this work were supported by CHPC of University of Utah and the High Performance Computing Platform of Peking University.

■ REFERENCES

(1) Žutić, I.; Fabian, J.; Das Sarma, S. *Rev. Mod. Phys.* **2004**, *76*, 323−410.
(2) Dyakonov, M. I.; Perel, V. I. *Sov. Phys. Solid State* **1972**, *13*, 3023−3026.
(3) Schliemann, J.; Egues, J. C.; Loss, D. *Phys. Rev. Lett.* **2003**, *90*, 146801.
(4) Bernevig, B. A.; Orenstein, J.; Zhang, S.-C. *Phys. Rev. Lett.* **2006**, *97*, 236601.
(5) Koralek, J. D.; Weber, C. P.; Orenstein, J.; Bernevig, B. A.; Zhang, S.-C.; Mack, S.; Awschalom, D. D. *Nature* **2009**, *458*, 610.
(6) Walser, M. P.; Reichl, C.; Wegscheider, W.; Salis, G. *Nat. Phys.* **2012**, *8*, 757.
(7) Rashba, E. I. *Sov. Phys. Solid State* **1960**, *2*, 1109.
(8) Dresselhaus, G. *Phys. Rev.* **1955**, *100*, 580−586.
(9) Kohda, M.; Lechner, V.; Kunihashi, Y.; Dollinger, T.; Olbrich, P.; Schönhuber, C.; Caspers, I.; Bel'kov, V. V.; Golub, L. E.; Weiss, D.; Richter, K.; Nitta, J.; Ganichev, S. D. *Phys. Rev. B: Condens. Matter Mater. Phys.* **2012**, *86*, No. 081306.
(10) Chen, Y. S.; Fält, S.; Wegscheider, W.; Salis, G. *Phys. Rev. B: Condens. Matter Mater. Phys.* **2014**, *90*, 121304.
(11) Kammermeier, M.; Wenk, P.; Schliemann, J. *Phys. Rev. Lett.* **2016**, *117*, 236801.
(12) Dettwiler, F.; Fu, J.; Mack, S.; Weigele, P. J.; Egues, J. C.; Awschalom, D. D.; Zumbühl, D. M. *Phys. Rev. X* **2017**, *7*, No. 031010.
(13) Iizasa, D.; Sato, D.; Morita, K.; Nitta, J.; Kohda, M. *Phys. Rev. B: Condens. Matter Mater. Phys.* **2018**, *98*, 165112.
(14) Schliemann, J. *Rev. Mod. Phys.* **2017**, *89*, No. 011001.
(15) Kohda, M.; Salis, G. *Semicond. Sci. Technol.* **2017**, *32*, No. 073002.
(16) Tao, L. L.; Tsymbal, E. Y. *Nat. Commun.* **2018**, *9*, 2763.
(17) Reshchikov, M. A.; Morkoç, H. *J. Appl. Phys.* **2005**, *97*, No. 061301.
(18) Lee, Y.-H.; Zhang, X.-Q.; Zhang, W.; Chang, M.-T.; Lin, C.-T.; Chang, K.-D.; Yu, Y.-C.; Wang, J. T.-W.; Chang, C.-S.; Li, L.-J.; Lin, T.-W. *Adv. Mater.* **2012**, *24*, 2320−2325.
(19) Yin, W.-J.; Yang, J.-H.; Kang, J.; Yan, Y.; Wei, S.-H. J. *J. Mater. Chem. A* **2015**, *3*, 8926−8942.
(20) Huang, J.; Yuan, Y.; Shao, Y.; Yan, Y. *Nat. Rev. Mater.* **2017**, *2*, 17042.
(21) Hu, L.; Huang, H.; Wang, Z.; Jiang, W.; Ni, X.; Zhou, Y.; Zielasek, V.; Lagally, M. G.; Huang, B.; Liu, F. *Phys. Rev. Lett.* **2018**, *121*, No. 066401.

DOI: 10.1021/acs.nanolett.9b01812
Nano Lett. 2019, 19, 6005−6012

(22) Tan, C.; Cao, X.; Wu, X.-J.; He, Q.; Yang, J.; Zhang, X.; Chen, J.; Zhao, W.; Han, S.; Nam, G.-H.; Sindoro, M.; Zhang, H. *Chem. Rev.* **2017**, *117*, 6225−6331.
(23) Manzeli, S.; Ovchinnikov, D.; Pasquier, D.; Yazyev, O. V.; Kis, A. *Nat. Rev. Mater.* **2017**, *2*, 17033.
(24) Komsa, H.-P.; Kurasch, S.; Lehtinen, O.; Kaiser, U.; Krasheninnikov, A. V. *Phys. Rev. B: Condens. Matter Mater. Phys.* **2013**, *88*, No. 035301.
(25) Lin, Z.; Carvalho, B. R.; Kahn, E.; Lv, R.; Rao, R.; Terrones, H.; Pimenta, M. A.; Terrones, M. *2D Mater.* **2016**, *3*, No. 022002.
(26) Tongay, S.; Zhou, J.; Ataca, C.; Lo, K.; Matthews, T. S.; Li, J.; Grossman, J. C.; Wu, J. *Nano Lett.* **2012**, *12*, 5576−5580.
(27) Chiu, M.-H.; Zhang, C.; Shiu, H.-W.; Chuu, C.-P.; Chen, C.-H.; Chang, C.-Y. S.; Chen, C.-H.; Chou, M.-Y.; Shih, C.-K.; Li, L.-J. *Nat. Commun.* **2015**, *6*, 7666.
(28) Hill, H. M.; Rigosi, A. F.; Rim, K. T.; Flynn, G. W.; Heinz, T. F. *Nano Lett.* **2016**, *16*, 4831−4837.
(29) Zhu, Z. Y.; Cheng, Y. C.; Schwingenschlögl, U. *Phys. Rev. B: Condens. Matter Mater. Phys.* **2011**, *84*, 153402.
(30) Kresse, G.; Furthmüller, J. *Phys. Rev. B: Condens. Matter Mater. Phys.* **1996**, *54*, 11169−11186.
(31) Blöchl, P. E. *Phys. Rev. B: Condens. Matter Mater. Phys.* **1994**, *50*, 17953−17979.
(32) Perdew, J. P.; Burke, K.; Ernzerhof, M. *Phys. Rev. Lett.* **1996**, *77*, 3865−3868.
(33) Monkhorst, H. J.; Pack, J. D. *Phys. Rev. B* **1976**, *13*, 5188−5192.
(34) Groth, C. W.; Wimmer, M.; Akhmerov, A. R.; Waintal, X. *New J. Phys.* **2014**, *16*, No. 063065.
(35) Wang, S.; Lee, G.-D.; Lee, S.; Yoon, E.; Warner, J. H. *ACS Nano* **2016**, *10*, 5419−5430.
(36) Chen, Q.; Li, H.; Zhou, S.; Xu, W.; Chen, J.; Sawada, H.; Allen, C. S.; Kirkland, A. I.; Grossman, J. C.; Warner, J. H. *ACS Nano* **2018**, *12*, 7721−7730.
(37) Hosoki, S.; Hosaka, S.; Hasegawa, T. *Appl. Surf. Sci.* **1992**, *60*−*61*, 643−647.
(38) Hosaka, S.; Hosoki, S.; Hasegawa, T.; Koyanagi, H.; Shintani, T.; Miyamoto, M. J. *J. Vac. Sci. Technol., B: Microelectron. Process. Phenom.* **1995**, *13*, 2813−2818.
(39) Naik, M. H.; Jain, M. *Phys. Rev. Mater.* **2018**, *2*, No. 084002.
(40) Refaely-Abramson, S.; Qiu, D. Y.; Louie, S. G.; Neaton, J. B. *Phys. Rev. Lett.* **2018**, *121*, 167402.
(41) Qiu, H.; Xu, T.; Wang, Z.; Ren, W.; Nan, H.; Ni, Z.; Chen, Q.; Yuan, S.; Miao, F.; Song, F.; Long, G.; Shi, Y.; Sun, L.; Wang, J.; Wang, X. *Nat. Commun.* **2013**, *4*, 2642.
(42) Fishchuk, I. I.; Kadashchuk, A.; Bhoolokam, A.; de Jamblinne de Meux, A.; Pourtois, G.; Gavrilyuk, M. M.; Köhler, A.; Bässler, H.; Heremans, P.; Genoe, J. *Phys. Rev. B: Condens. Matter Mater. Phys.* **2016**, *93*, 195204.
(43) Vajna, S.; Simon, E.; Szilva, A.; Palotas, K.; Ujfalussy, B.; Szunyogh, L. *Phys. Rev. B: Condens. Matter Mater. Phys.* **2012**, *85*, No. 075404.
(44) Datta, S.; Das, B. *Appl. Phys. Lett.* **1990**, *56*, 665−667.
(45) Huang, B.; Jin, K.-H.; Cui, B.; Zhai, F.; Mei, J.; Liu, F. *Nat. Commun.* **2017**, *8*, 15850.
(46) Schönhuber, C.; Walser, M. P.; Salis, G.; Reichl, C.; Wegscheider, W.; Korn, T.; Schüller, C. *Phys. Rev. B: Condens. Matter Mater. Phys.* **2014**, *89*, No. 085406.
(47) Koo, H. C.; Kwon, J. H.; Eom, J.; Chang, J.; Han, S. H.; Johnson, M. *Science* **2009**, *325*, 1515.
(48) Matos-Abiague, A.; Fabian, J. *Phys. Rev. Lett.* **2015**, *115*, No. 056602.
(49) Tao, L. L.; Paudel, T. R.; Kovalev, A. A.; Tsymbal, E. Y. *Phys. Rev. B: Condens. Matter Mater. Phys.* **2017**, *95*, 245141.
(50) Zhuravlev, M. Y.; Alexandrov, A.; Tao, L. L.; Tsymbal, E. Y. *Appl. Phys. Lett.* **2018**, *113*, 172405.

DOI: 10.1021/acs.nanolett.9b01812
Nano Lett. 2019, 19, 6005−6012